

Spectroscopic and kinematic analyses of a warm survivor of a D⁶ supernova

M. A. Hollands,¹★ K. J. Shen,² R. Raddi³, B. T. Gänsicke,¹ E. B. Bauer,⁴ and A. Rebassa-Mansergas^{3,5}

¹ Department of Physics, University of Warwick, Coventry, CV4 7AL, UK

² Department of Astronomy and Theoretical Astrophysics Center, University of California, Berkeley, CA 94720, USA

³ Departament de Física, Universitat Politècnica de Catalunya, c/Esteve Terrades 5, 08860 Castelldefels, Spain

⁴ Center for Astrophysics | Harvard & Smithsonian, 60 Garden St., Cambridge, MA 02138, USA

⁵ Institut d'Estudis Espacials de Catalunya, Esteve Terradas, 1, Edifici RDIT, Campus PMT-UPC, 08860 Castelldefels, Barcelona, Spain

Accepted 2025 June 09. Received 2025 June 09; in original form 2025 April 11

ABSTRACT

SDSS J163712.21+363155.9 is a candidate hyper-runaway star, first identified from its unusual spectrum in the Sloan Digital Sky Survey, which exhibits oxygen, magnesium, and silicon lines redshifted by several 100 km s^{−1}, leading to the suggestion it was ejected from a thermonuclear supernova. We have acquired GTC OSIRIS spectroscopy of SDSS J1637+3631 establishing a warm ($T_{\text{eff}} = 15\,680 \pm 250$ K) carbon+oxygen dominated atmosphere, that is also abundant in the intermediate mass elements silicon, sulphur, and calcium. We interpret SDSS J1637+3631 as the donor to an accreting white dwarf that exploded in a dynamically-driven double-degenerate double-detonation (D⁶) type Ia supernova, where the current composition is consistent with a CO white dwarf core, enriched with intermediate mass elements from deposited supernova ejecta. While SDSS J1637+3631 has a low-precision *Gaia* parallax, our spectroscopic surface gravity ($\log g = 6.3 \pm 0.3$ dex) helps constrain its tangential velocity to 1950^{+810}_{-530} km s^{−1}, providing additional support to the D⁶ mechanism. Under the assumption that SDSS J1637+3631 is a D⁶ survivor, we construct a kinematic model combining all astrometric, spectroscopic, and photometric information, but also including the structure and gravitational potential of the Milky Way. Our model localises the ejection site to the inner few kpc of the Galactic disc (though excluding the Galactic centre), with an ejection speed of 1870^{+360}_{-300} km s^{−1}, and a $4.5^{+0.4}_{-0.5}$ Myr time of flight.

Key words: (*stars:*) supernovae: general – (*stars:*) white dwarfs – stars: abundances – stars: kinematics and dynamics

1 INTRODUCTION

Type Ia supernovae result from the thermonuclear detonation of a white dwarf, the stellar remnant left behind by the vast majority of main sequence stars. For a white dwarf to undergo such a destructive process requires a high enough density to trigger carbon fusion within the interior (Khokhlov 1991). These conditions can be achieved when the white dwarf is part of a multiple star system, either by accretion from or by a merger with a companion (where the companion may also be a white dwarf). As astrophysical transients, type Ia supernovae can easily outshine their host galaxies, permitting their use as standardisable candles for measuring cosmic distances, which led to the discovery that the expansion of the universe is accelerating (Riess et al. 1998; Perlmutter et al. 1999). Despite their importance in cosmology, several open questions remain regarding type Ia supernovae, primarily the specific channels that lead to their occurrence (Wang & Han 2012; Ruiter & Seitzzahl 2025), the relative rates at which these channels occur, and how the yields influence the chemical evolution of the universe (Thielemann et al. 1986).

Over the last decade it has become clear that in some cases, white dwarfs or their companions can survive type Ia supernovae, providing

new avenues to study them. Evidence for such supernova survivors has come from extragalactic observations of peculiar supernovae (McCully et al. 2014), theoretical predictions from supernova modelling, and finally the observation of chemically and/or kinematically peculiar stars within the Milky Way galaxy. Such peculiar stars that have been found within the Milky Way are reviewed below.

The first Galactic star proposed to be the survivor of a supernova is US 708, which was found by Geier et al. (2015) to be a helium-rich hot subdwarf moving faster than 1000 km s^{−1}, making it the fastest known unbound stellar object in the Galaxy at that time. Hypervelocity stars, i.e. stars unbound to the Milky Way, were previously understood to be ejections from the Galactic centre (Hills 1988; Koposov et al. 2020). Although US 708 lacked a parallax at that time, the other proper-motion and radial velocity were sufficient to show that a Galactocentric origin was highly improbable. This, along with the discovery that US 708 is a rapid rotator led Geier et al. (2015) to conclude that this subdwarf was the donor to a white dwarf which exploded as a type Ia supernova, where the donor survived, and was ejected from the disrupted binary system.

Observations of extragalactic transients identified a class of peculiar underluminous type Ia (Li et al. 2003; Jha et al. 2006), termed type Iax (Foley et al. 2013). These transients were proposed to originate from the deflagration of a white dwarf accreting from a helium-rich

★ E-mail: mark.hollands@warwick.ac.uk

companion (e.g. similar to US 708). Simulations of such deflagrations were found to leave behind a bound-remnant (Kromer et al. 2013; Fink et al. 2014; Jones et al. 2019), leading to the possibility that partially burned stars could exist in the Milky Way and may be identified by their unusual compositions and kinematics. The first object discovered fitting this description was LP 40–365 (GD 492) by Vennes et al. (2017). LP 40–365 is found to have a neon dominated atmosphere and has a spectrum populated with metal lines from a variety of elements, as well as a radial velocity of $\approx 500 \text{ km s}^{-1}$. The resemblance to an exposed ONe white dwarf core, potentially enhanced in supernova burning products with a super-solar Mn/Fe ratio (Raddi et al. 2018a), indicated a near-Chandrasekhar mass deflagration (Seitenzahl et al. 2013). With the release of *Gaia* data release 2 (DR2), LP 40–365 could be placed on the Hertzsprung-Russell diagram (HRD), where it was found to reside between the white dwarf and main sequences (Raddi et al. 2018b), implying a low mass and inflated radius compared to normal white dwarfs, but more compact than main sequence stars of a similar temperature. Additional objects in the same spectral class as LP 40–365 have since been identified with similar compositions and high-speed kinematics (Raddi et al. 2019; El-Badry et al. 2023).

One process predicted to lead directly to standard type Ia supernovae is the double-detonation mechanism (Taam 1980; Livne 1990). In a double-detonation supernova, an accreting white dwarf primary (which may have a mass well below the Chandrasekhar-limit; Fink et al. 2007, 2010) undergoes an initial detonation in its helium envelope (Shen et al. 2009), where the helium burning shock front travels around the stellar surface and is focussed onto the opposite side, triggering a second detonation of the carbon in the white dwarf core (Shen & Bildsten 2014). In double-degenerate systems, where the Roche-lobe filling donor star is also a white dwarf (which could harbour either a He core or a CO core with a He-rich envelope), double detonations are expected to occur (Guillochon et al. 2010; Dan et al. 2011; Raskin et al. 2012; Pakmor et al. 2013), and can potentially lead to another kind of supernova survivor: Although the primary white dwarf is destroyed, the donor may survive interaction with the supernova shock, being flung out of the system (Shen et al. 2018) with approximately its orbital velocity. This type of supernova has been termed the dynamically-driven double-degenerate double-detonation (D^6) mechanism, and can potentially occur in all CO-core white dwarfs with masses below $1 M_{\odot}$ (Shen et al. 2024). While double detonations offer the potential to explain a large fraction of all type Ia supernovae (Ruiter & Seitenzahl 2025), searches within/around supernova remnants for surviving donors have proved unsuccessful (Shen et al. 2018; Shields et al. 2023). Another challenge for the D^6 mechanism is matching the estimated Galactic supernova rate to the number of known survivors (El-Badry et al. 2023). However, recent work has shown that interaction between the ejecta and donor can trigger a further double detonation, destroying both stars, (Tanikawa et al. 2019; Pakmor et al. 2022; Boos et al. 2024), and with Shen (2025) indicating this occurs in the majority of cases, where only a few percent of systems leave behind surviving donors.

A defining observational signature for the survivors of D^6 supernovae, simply referred to as D^6 stars, is their huge ejection velocities which are expected between 1000 to 3000 km s^{-1} (Shen et al. 2018). Having interacted with the high-velocity supernova ejecta, the donor is expected to have undergone mass loss due to stripping of its envelope, which may further be chemically enhanced by ejecta material accreted during the explosion. D^6 stars are therefore also expected to have unusual spectra that may be dominated with carbon and oxygen from the exposed white dwarf core, but enhanced with traces of heavier metals.

With the release of *Gaia* DR2, Shen et al. (2018), searched for stars with extreme tangential velocities (v_{\perp}) exceeding 1000 km s^{-1} , following up with low-resolution spectroscopy. Of their seven candidates, four turned out to be ordinary stars with probable underestimated parallaxes. However, the remaining three (named D6-1, D6-2, and D6-3) had unusual (but mutually similar) spectra dominated by atomic lines from oxygen and carbon C_2 molecular bands, as well as metal lines from magnesium and calcium. All three had estimated $T_{\text{eff}} \approx 8000 \text{ K}$, and their sharp Ca II H+K lines established D6-1 to have a radial velocity of 1200 km s^{-1} — though curiously D6-2 and D6-3 had radial velocities consistent with zero. The past trajectory of D6-2 was also found to coincide with the supernova remnant G70.0-21.5. Evidently these stars match the expected properties of D^6 survivors, though to date are yet to receive dedicated spectral analyses of their atmospheres (Hollands et al., in prep). Similar searches for high v_{\perp} objects with precise measurements in *Gaia* DR3 did not reveal any new D^6 candidates (Igoshev et al. 2023), and constructing clean searches for hyper-runaway stars has been shown to be a complex task (Scholz 2024).

With the lowest hanging fruit already discovered by Shen et al. (2018), El-Badry et al. (2023) identified four more D^6 stars by searching for blue objects with low parallax significance, but still with sizeable proper-motions. Unlike the cool stars found by Shen et al. (2018), these new discoveries were much hotter, with most having $T_{\text{eff}} > 60\,000 \text{ K}$. The atmospheres of these hottest stars were first analysed by Werner et al. (2024a) identifying carbon and oxygen rich atmospheres for two of them, with a third having a more typical DAO white dwarf spectrum. One of these objects, J0927–6335, has been followed up with ultraviolet observations (Werner et al. 2024b), establishing an atmosphere not only rich in carbon and oxygen, but also enhanced in silicon, iron and nickel. However, the authors acknowledge that the abundances of these hot D^6 stars may be affected by radiative levitation, and that the effect of gravitational settling is not known for these stars.

1.1 SDSS J1637+3631

Following the second data release of *Gaia*, Raddi et al. (2019) presented the discovery of additional stars in the same class as LP 40–365. Two objects were identified from their position in the HRD, large tangential velocities, and subsequent follow-up spectroscopy. Having found these stars to have distinctive spectra dominated by strong magnesium and oxygen lines, the authors searched the Sloan Digital Sky Survey (SDSS) spectroscopic database for additional LP 40–365-like candidates that may have been observed serendipitously. Using a grid of LP 40–365-like templates at different T_{eff} and radial velocity, the authors identified three objects with peculiar spectra.

The first of these was a known white dwarf (Kepler et al. 2016), SDSS J1240+6710, which has a unique oxygen dominated atmosphere, and has been suggested to have formed from a thermonuclear burning event distinct from the mechanisms producing the D^6 and LP 40–365 remnants (Gänsicke et al. 2020).

The second object, SDSS J0905+2510, was found to closely match one of the LP 40–365 templates, adding a fourth member to the class of LP 40–365 stars known at that time. SDSS J0905+2510 could not have been identified using the astrometric approach, as its *Gaia* DR2 record did not have an available parallax or proper-motion.¹

¹ J0905+2510 now has full 5-parameter astrometry in *Gaia* DR3, though its parallax is measured to less than 1σ precision ($0.2879 \pm 0.4987 \text{ mas}$).

Parameter	value
Gaia DR3 source ID	1327920737357113088
RA (J2016)	16:37:12.214
Dec (J2016)	+36:31:55.91
ϖ [mas]	0.3319 ± 0.4776
μ_{RA} [mas yr $^{-1}$]	-19.558 ± 0.587
μ_{Dec} [mas yr $^{-1}$]	$+64.159 \pm 0.644$
<i>Gaia</i> G	20.2549 ± 0.0063
<i>Gaia</i> G_{BP}	20.0409 ± 0.0698
<i>Gaia</i> G_{RP}	20.1670 ± 0.1319
SDSS u	20.008 ± 0.053
SDSS g	20.092 ± 0.021
SDSS r	20.399 ± 0.039
SDSS i	20.623 ± 0.064
SDSS z	20.861 ± 0.282
PanSTARRS g	20.1335 ± 0.0108
PanSTARRS r	20.4299 ± 0.0127
PanSTARRS i	20.6833 ± 0.0287
PanSTARRS z	20.8248 ± 0.0389

Table 1. Astrometry and photometry for SDSS J1637+3631.

The final peculiar object found by (Raddi et al. 2019) using their template fitting approach is the star SDSS J163712.21+363155.9 (SDSS J1637+3631 hereafter), and is the primary subject of this work. SDSS J1637+3631 appeared to be hotter than the other objects analysed by Raddi et al. (2019), best-matching the hottest template in their grid (20 000 K). The star was found to match several velocity-shifted ($\approx 300 \text{ km s}^{-1}$) metal lines in the template, arising from Mg II, O I, and Si II. Even so, other lines were found to be present in the data that were either absent or much weaker in the template, such as the Ca II H+K lines, and further O I lines. SDSS J1637+3631, was therefore considered unlikely to originate from the same mechanism as the other stars in the LP 40–365 class, and may instead belong to one of the other exotic classes of remnants related to white dwarf supernovae, such as the aforementioned oxygen-rich white dwarf SDSS J1240+6710, or surviving donors of the D^6 supernovae. However, its origin could not be revealed from its *Gaia* astrometry, as its DR2 parallax of $0.39 \pm 0.60 \text{ mas}$ (now revised to $0.33 \pm 0.48 \text{ mas}$ in DR3: see Table 1 for all DR3 astrometry and available optical photometry) was insufficiently precise to establish either its location in the *Gaia* HRD or determine the magnitude of its tangential velocity, v_{\perp} (though the 67 mas yr^{-1} hinted at a fast moving star).

In this work, we provide new spectroscopic observations and analysis of SDSS J1637+3631, establishing that this elusive object is the ejected donor from a D^6 supernova. In section 2, we present our spectroscopic observations of SDSS J1637+3631. In section 3 we perform a detailed spectral analysis of our observations, establishing a C+O dominated composition enhanced with heavier elements such as Si and Ca. In section 4, we combine several pieces of information to conclude that SDSS J1637+3631 is the surviving donor from a D^6 explosion. In section 5, we take these arguments further to determine the kinematic properties of SDSS J1637+3631, its likely birth site, and time-of-flight. Finally, we present our conclusions in section 6.

2 SPECTROSCOPIC OBSERVATIONS

We obtained follow up spectroscopy of SDSS J1637+3631 using the OSIRIS (Optical System for Imaging and low-Intermediate-Resolution Integrated Spectroscopy) instrument mounted on the

Gran Telescopio CANARIAS (GTC) at the Roque de los Muchachos observatory on La Palma. These observations were performed in service mode on the night starting 2019 June 08 under photometric observing conditions and seeing of 0.7 arcsec. To obtain broad spectral coverage across the optical at intermediate resolution, we used three instrumental setups with the R2500U, R2500V, and R2500R VPH gratings, all with a 0.6 arcsec slit width. This gave continuous spectral coverage over the range 3440–7685 Å, with a resolving power of $R \approx 2500$ in all three gratings. For both the R2500U and R2500V gratings, 1 hour of integration time was acquired over three sub-exposures each (i.e. 1200 s per exposure). For the R2500R grating, we opted for six 1200 s exposures totalling 2 hours of integration time. The additional exposure time for R2500R was chosen because SDSS J1637+3631 is intrinsically blue and the detection of neon (a key element in the atmospheres of SDSS J1240+6710 and the LP 40–365 stars) from weak Ne I lines (6144/6404/6508 Å being the strongest) would depend on having a higher spectral signal-to-noise ratio (at least 30) than would be necessary at bluer wavelengths.

Standard calibration data were acquired with flat field frames and arc lamp exposures (for all three gratings) taken at the end of the night. The provided bias frames were taken at the start of the following night (2019-06-09). The DA white dwarf GD 153 was observed as a spectral flux standard shortly before our science observations were taken and at a similar airmass to the target (≈ 1.05).

We performed reduction of the data using the STARLINK package of software (Currie et al. 2014; Bell et al. 2024), which included bias subtraction, flat fielding, and optimal extraction (Horne 1986; Marsh 1989) of the spectra with each grating. Wavelength and flux calibrations (including telluric removal) were performed using MOLLY.² Sub-exposures of each band were combined by weighted averaging, with the three bands merged into a single spectrum, averaging similarly over the overlapping regions. The final coadded spectrum is shown in Figure 1 (top panel).

3 SPECTROSCOPIC ANALYSIS

Our new GTC spectrum allowed us to identify many more elements in the atmosphere of SDSS J1637+3631 than was possible with the SDSS spectrum, owing to the much higher signal-to-noise ratio. In addition to the previously identified lines of O I, Mg II, Si II, and Ca II (Raddi et al. 2019), we also identified lines from C I–II, O II, Ne I, Al I, Si I, S I–II, and Fe II (see labelled panels in Figure 1). No lines of hydrogen or helium were detected. Arguably the most important of these identifications is carbon, which despite being undetectable in the SDSS spectrum, shows many strong lines and blends (such as the deep blend near a rest wavelength of 7115 Å) indicating this element constitutes a large proportion of the atmosphere. Like in the LP 40–365-stars, neon is detected, but despite being much hotter (leading to higher excitation of optical Ne I transitions), the lines are not as strong as in the Ne-dominated atmospheres of the LP 40–365-stars, indicating that this element is not as abundant in SDSS J1637+3631. In addition to these newly detected elements, the spectrum allowed us to measure a radial velocity of $384 \pm 6 \text{ km s}^{-1}$, confirming the fast kinematics suggested by the template fitting of the SDSS spectrum.

To model our GTC spectrum of SDSS J1637+3631, we used the latest version of the Koester white dwarf model atmosphere code

² MOLLY can be found at <https://cygnus.astro.warwick.ac.uk/phsaap/software/>

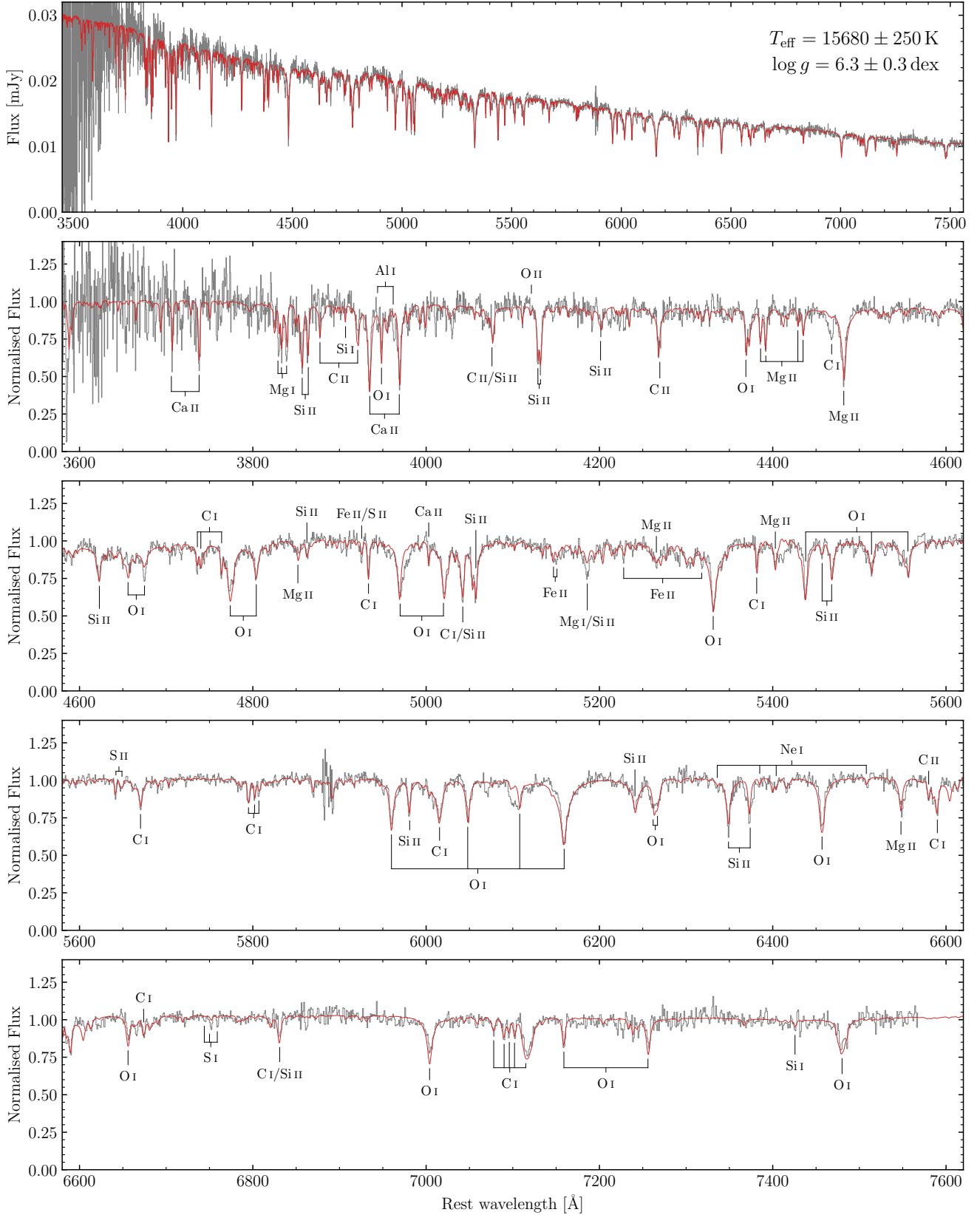


Figure 1. GTC OSIRIS spectrum of SDSS J1637+3631 (grey) with best fitting model (red). The top panel shows the entire GTC dataset in physical flux units. Subsequent panels show portions of the spectral range with fluxes normalised to one, and with labelled spectral features. All panels are in vacuum wavelengths with the data shifted to the rest frame.

(Koester 2010). Compared to normal metal-rich white dwarfs, which may only require the inclusion of hundreds to thousands of metal lines, the apparently pure metal atmosphere of SDSS J1637+3631 required tens of thousands of lines from all detected elements. Owing to the warm T_{eff} of SDSS J1637+3631 (a preliminary fit indicated a value of $\approx 16\,000$ K), more than half of the integrated flux is emitted at ultraviolet wavelengths, a region which is densely populated with metal transitions. While the majority of these lines are narrow (full width half maxima of a few $0.01\,\text{\AA}$) and therefore contribute negligible opacity on an individual basis, there are so many thousands of such lines (of which a large fraction are saturated in the line cores, though still almost vanish when convolved to the instrumental resolution), that excluding these weak lines en masse would still cause a drastic reduction in the total atmospheric opacity. Therefore all lines used in this analysis were included in both the atmospheric structure calculation and spectral synthesis. As a result, our calculations had to be evaluated on a dense wavelength grid in order to properly sample the lines at all stages of the model calculation. For the continuous opacity, we included bound-free photoionisation cross-sections (Cunto et al. 1993) of C, O, Ne, Mg, Al, Si, S, Ca, and Fe, and with all but Ne including the first two ionisation stages. Additionally, the Koester models automatically include bound-free and free-free opacities for the negative ions C^- and O^- , and the free-free opacity for Ne^- , when those elements are present in the calculation. However at the temperature of SDSS J1637+3631 these negative ions were found to have a negligible contribution compared to the aforementioned bound-free cross-sections. While we did test our models with molecular abundances included, at this temperature the most abundant molecular species: CO^+ , O_2^+ and CO were present at number fractions below 10^{-7} . As such, including them had a negligible effect on the atomic number abundances nor on the emergent flux from molecular opacities. Therefore molecules were excluded from our fitting to reduce the computation time. All fluxes in the atmospheric structure calculation were converged to 0.1 per cent accuracy.

Because of the large number of free parameters, and because the models were expensive to compute compared to typical white dwarf atmospheres, it was infeasible to construct multidimensional model grids for our fitting procedure. We therefore performed a least squares fit to the spectrum with T_{eff} , $\log g$, and the chemical abundances (relative to carbon) as free parameters, recalculating the model at each step in the procedure. At each step in the fit, the model was velocity shifted to the previous measurement of $384\,\text{km s}^{-1}$, and convolved to the instrumental resolving power of 2500. To scale the model to the observed fluxes we took the ratio of the data and model and fit a 5th order polynomial across the entire wavelength range, then multiplying the model by this wavelength dependent polynomial. This procedure accounts for the unknown solid angle, interstellar extinction, and uncertainty in flux calibration.

While we quickly established that oxygen is the most abundant element by number, we found that the bound-free opacity of atomic carbon dominates the continuum opacity from 1000 to 4000 \AA , where around 80 percent of the integrated flux is emitted. We therefore chose carbon for the denominator of abundance ratios, reducing the degree of correlation between abundances. Had oxygen been used for this purpose, varying $\log(\text{C}/\text{O})$ with other abundances held constant relative to oxygen causes the line strengths of unrelated metals to also vary (whereas varying $\log(\text{O}/\text{C})$ with other abundances held constant relative to carbon does not have such an effect). For redder wavelengths, the atomic carbon and atomic oxygen bound-free opacities are roughly equal up to $\approx 6000\,\text{\AA}$, after which point the oxygen photoionisation opacity dominates. Beyond 9000 \AA metal free-free opacities overtake the metal bound-free opacities.

While the best fitting model from this process showed generally good agreement with the data (Figure 1, red), the formal uncertainties were unrealistically small, i.e. 50 K in T_{eff} , and a few 0.01 dex in all other parameters. To better estimate the uncertainties, we constructed 1-dimensional grids of models for each parameter around the best fitting values. For T_{eff} this meant models spanning -1000 to $+1000$ in steps of 50 K around the best fitting value, and for $\log g$ and chemical abundances 1 dex above and below the best fitting value in steps of 0.05 dex. These grids were visually compared against the data to determine our quoted uncertainties. For the surface gravity this was more complex than for normal white dwarfs, where typically the $\log g$ is inferred from the pressure broadening of the hydrogen or helium lines. Instead we found that increasing the $\log g$ changed the strengths of many different metal lines from a variety of elements simultaneously, with some becoming stronger and others weaker, leading to a higher uncertainty than for normal white dwarfs.

We used a similar approach to determine upper-limits for hydrogen and helium, constructing grids spanning many orders of magnitude in steps of 0.5 dex. We then used the Bayesian approach developed by Hollands et al. (2020) (i.e. using a Jeffreys prior, $P(Z) \propto 10^{Z/2}$, where $Z = \log(\text{H}(\text{e})/\text{C})$) to determine the 99th percentile upper-limits of $\log(\text{H}/\text{C}) < -4.1$ dex and $\log(\text{He}/\text{C}) < -1.5$ dex respectively. As nickel is an important element synthesised in type Ia supernovae, we used the same approach to determine an upper-limit of $\log(\text{Ni}/\text{C}) < -2.9$ dex focussing on a strong (unresolved) Ni I doublet at 5082 \AA . We note that stronger Ni I lines are expected at wavelengths between 3400–3600 \AA (bluer than is covered by our GTC spectrum), which may permit an improved upper-limit or measurement in the future.

Evidence for rotation has been observed for supernova bound remnants in the past for both the LP 40–365 (Hermes et al. 2021) and D^6 (Chandra et al. 2022) classes of stars. In both cases, rotational periods on the order of ~ 10 hours are inferred from time-series photometry. While we do not currently have time-series photometry available for SDSS J1637+3631, it is still possible to place constraints on rotation via broadening of spectral lines. We found no evidence for rotational broadening of the spectrum, with an inferred upper-limit of $v \sin i < 40\,\text{km s}^{-1}$. Indeed for a 10 hr rotation period and radius of $0.1\,R_{\odot}$ (which is close to the actual radius inferred in later sections), the $14\,\text{km s}^{-1}$ equatorial rotation speed would be well below our detection threshold for our $R = 2500$ spectra.

Our best fitting spectroscopic parameters and their uncertainties (or upper-limits) are presented in Table 2. The best fitting model is shown in all panels of Figure 1 demonstrating good agreement in the majority of lines. We note that a few of the strongest oxygen lines are slightly too broad (such as the 5331 \AA line), whereas others (such as the 4970 \AA line) are slightly too narrow, suggesting that improved broadening constants may be needed for more accurate modelling. SDSS J1637+3631 also shows a strong feature of C I near 4470 \AA which appears only weakly in our model. This line blend has been observed in other carbon-rich atmospheres (Hollands et al. 2020; Kilic et al. 2024), showing a similar discrepancy, suggesting improvements to the oscillator strengths of these lines are required. Similarly, absorption is also missing from our model near the 6107 \AA O I line and 5403 \AA Mg II line blend, indicating some additional minor opacities are required (which may or may not be related to the partially overlapping lines mentioned above). We have no reason to believe these missing or underestimated lines will affect our estimated atmospheric parameters.

Parameter	value
T_{eff}	$15\,680 \pm 250$ K
$\log g$	6.3 ± 0.3 dex(cm s^{-2})
v_r	384 ± 6 km s^{-1}
$v \sin i$	< 40 km s^{-1}
H	< -4.1 dex
He	< -2.0 dex
O	$+0.27 \pm 0.10$ dex
Ne	-1.86 ± 0.25 dex
Mg	-2.33 ± 0.15 dex
Al	-4.00 ± 0.30 dex
Si	-1.76 ± 0.10 dex
S	-2.84 ± 0.30 dex
Ca	-2.85 ± 0.10 dex
Fe	-3.00 ± 0.20 dex
Ni	< -2.9 dex

Table 2. Atmospheric parameters for SDSS J1637+3631 determined from our spectroscopic fitting. Abundances are logarithmic number ratios relative to carbon.

3.1 Chemical abundance interpretation

The abundances in Table 2 reveal an object dominated by carbon and oxygen in a roughly 1:2 ratio. The atmosphere also contains moderate traces of other light elements, i.e. Ne, Mg, and Al, as well as heavier elements, i.e. Si, S, Ca, and Fe. These atmospheric abundances are shown in Figure 2 (top), normalised to the total abundance (by number), and compared with other chemically peculiar white dwarfs. J0927–6335 is the hot D⁶ star discovered by (El-Badry et al. 2023) and analysed by (Werner et al. 2024b) from its UV spectrum (their results shown here). SDSS J1240+6710 is the oxygen-rich white dwarf first identified by Kepler et al. (2016), and with a more detailed spectroscopic analysis performed by Gänsicke et al. (2020) (their results shown here). J1603–6613 is one of the LP 40–365-stars analysed by Raddi et al. (2019), and has the most elements detected for any LP 40–365-star so far. The three LP 40–365-stars analysed by (Raddi et al. 2019) have remarkably consistent abundances, and so we take J1603–6613 as a representative member of the LP 40–365-class. Neither hydrogen nor helium are detected in any of the four objects, with upper-limits ruling out these elements as major atmospheric constituents (a hydrogen upper-limit is not provided for J0927–6335, though at its high T_{eff} , a non-detection rules out hydrogen as a major atmospheric component, Werner et al. 2024a), with particularly good limits measured for SDSS J1637+3631.

While all four stars share oxygen as a major atmospheric constituent, only SDSS J1637+3631 and J0927–6335 also have carbon comprising a large fraction of their atmospheres, indicating that SDSS J1637+3631 is unrelated to the other two stars. Furthermore, SDSS J1637+3631 is depleted in neon, magnesium, and aluminium compared to SDSS J1240+6710 and J1603–6613, but instead shows higher abundances for heavier elements, with a particularly striking spike for silicon, representing around 1 percent of the atmosphere, comparable to that measured for J0927–6335. However, SDSS J1637+3631 and J0927–6335 differ by around 2 dex for iron, and by at least 1.2 dex for nickel, though at the much higher T_{eff} of J0927–6335, radiative levitation may be responsible for the atmospheric enhancement of these abundances (Werner et al. 2024b).

As well as similarities to J0927–6335, the C+O dominated atmosphere of SDSS J1637+3631 is superficially similar to the carbon and oxygen rich spectra reported for the prototype D⁶ stars (Shen et al.

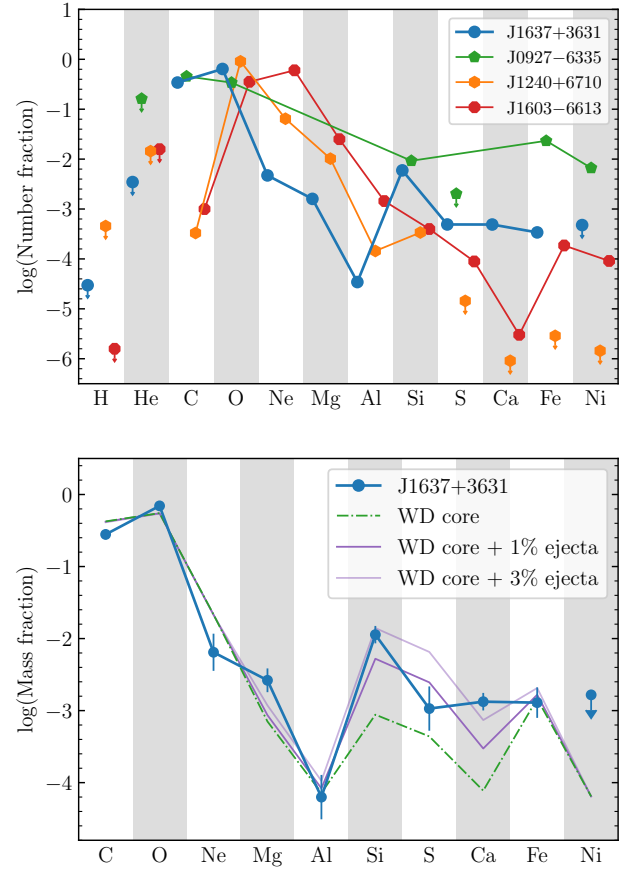


Figure 2. *Top:* Atmospheric number fractions for SDSS J1637+3631 (blue circles) compared with the hot D⁶ star, J0927–6335 (green pentagons); the oxygen-rich white dwarf, SDSS J1240+6710 (orange hexagons); and one star in the LP 40–365 class, J1603–6613 (red octagons). *Bottom:* Atmospheric mass fractions of SDSS J1637+3631 compared with the predicted core composition for a 0.57 M_{\odot} white dwarf (green dot dash), and the same model but with 1 and 3 per cent mass added from D6 ejecta.

2018). SDSS J1637+3631 may therefore be a surviving D⁶ remnant, where the present day abundances reflect the former donor white dwarf core composition (with the outer envelope stripped by supernova shocks), and then enhanced in heavier elements deposited from the supernova ejecta. Using a MESA model for a 3 M_{\odot} star evolved up to the formation of a carbon-oxygen core (see Shen (2025) for further details), we took the central composition as representative of the unaltered composition of a D⁶ donor which Shen (2025) have suggested are fully convective (and therefore chemically homogeneous) stars. These data (Figure 2, bottom) show generally consistent agreement from carbon up to aluminium, but also for Fe. For intermediate mass elements (IMEs) – specifically, silicon, sulphur, and calcium – our observations show clear enhancement compared to the expected white dwarf CO core composition. These IMEs are also expected to be highly abundant in the ejecta of D⁶ supernovae, particularly for velocities between 10 000 to 20 000 km s^{-1} (Boos et al. 2021). Importantly however, the low velocity material is dominated by radioactive nickel, which is not seen in the form of an Fe-excess.

We considered a simple model for the abundances of SDSS J1637+3631, where the CO core of the donor was enhanced with supernova ejecta, with elements impacting the donor in reverse

order of the ejecta velocity, i.e. where the fastest ejecta becomes buried by each successive layer. Since the nickel-rich outer most layers will be only marginally bound to the inflated donor, radioactive decay powered winds (Shen & Schwab 2017; Bhat et al. 2025) are then assumed to remove most of this element, with any remainder decaying to iron. Finally, as SDSS J1637+3631 evolves to a fully convective star, these ejecta abundances are mixed homogeneously within the initial core material. Of course this model is only an approximation, as it does not consider time-dependent mixing within the donor envelope, nor does it include detailed calculations for the fraction of each element removed via ^{56}Ni decay driven winds.

Boos et al. (2021) performed 2D simulations of white dwarf double detonations and their ejecta, with a variety of white dwarf masses and helium shell thicknesses. We took their 1 M_\odot model (for the exploding primary) using the thinnest helium shell value (specifically their `2d_decayed_ejecta_t35e7_d2e5_m100_v500` data), and for simplicity assumed equatorial ejection abundances. The abundances are provided as mass fractions as a function of velocity, $f_Z(v)$, and with the ejecta density, $\rho(v)$, also given. The fastest material has low density and should therefore contribute very little to the accreted total. On the other hand, the slowest material has high density, but as stated previously, is nickel-rich. Since we do not observe significant iron-enrichment, we therefore assumed that material with nickel fractions above 10 percent were removed via decay powered winds, corresponding to a minimum velocity of $11\,000\text{ km s}^{-1}$. For a given element, Z , the integrated total is then given by

$$I_Z = \int_{11}^{45} f_Z(v)\rho(v) dv, \quad (1)$$

where v is in units of 1000 km s^{-1} and the data by Boos et al. (2021) are calculated up to $45\,000\text{ km s}^{-1}$. Of course the magnitude and units of these integrals are arbitrary, and would require the donor cross-sectional area and accretion timescale, to directly calculate the integrated mass. However as we are specifically interested in their ratios, the mass fractions of the accreted ejecta, F_Z , are given by $F_Z = I_Z / \sum_k I_k$.

To determine the present day atmospheric abundances, we combined the core and ejecta abundances according to $F_{Z,\text{atm}} = (1 - q)F_{Z,\text{core}} + qF_{Z,\text{ejecta}}$, where q is the ejecta mass-fraction of the combined core and ejecta material. Our results are shown in Figure 2 (bottom) for values of $q = 0.01$ and $q = 0.03$. For 1 percent accreted ejecta, a mediocre compromise is seen for silicon, sulphur, and calcium compared to the observed abundances of SDSS J1637+3631. For 3 percent ejecta, good agreement is seen between for both silicon and calcium. However, the sulphur abundance is over-predicted by 0.7 dex, more than 2σ above the measurement.

One possible explanation is that systematic uncertainty in the modelling has lead to this (weakly detected) element to be underestimated. In Figure 1, the S II lines near 5650 \AA are well modelled, whereas the S I lines near 6750 \AA are clearly underestimated in strength. Increasing the atmospheric sulphur abundance by 0.7 dex provides a reasonable estimate for the strength of those S I lines without any substantial over-prediction of the 5650 \AA S II equivalent widths. However, a +0.7 dex abundance also results in additional sulphur lines appearing in our model which are not observed in the data, such as S II lines at 4164 \AA and 5214 \AA . Therefore the abundance provided in Table 2 provides a best compromise from our fitting procedure.

The quality of the atomic data in NIST (Kramida et al. 2024) is rated C+ (≤ 18 percent accuracy) for the 5650 \AA S II lines, whereas the 6750 \AA lines are rated D+ (≤ 40 percent accuracy). The other strong sulphur lines covered by our data have accuracy ratings rang-

ing from C+ to E (> 50 percent accuracy). Alternatively, the yields calculated by Boos et al. (2021) may simply over-predict the amount of sulphur produced by double-detonations. Either way, improved oscillator strengths for optical S I-II transitions will help to resolve this discrepancy.

While we have shown results from one specific dataset in Figure 2, Boos et al. (2021) provide a variety of data for calculations over a range of primary white dwarf masses, temperatures, and helium shell thicknesses. Experimenting with the other provided yield data, we found that the F_Z ratios are fairly consistent across all calculations, with F_S/F_{Si} between 0.46–0.50, and $F_{\text{Ca}}/F_{\text{Si}}$ between 0.05–0.07.

Our assumption that nickel is removed from the donor by radiation powered winds was motivated by the relative absence of iron, which would otherwise be expected to dominate the accreted ejecta abundances. This led to the conclusion that SDSS J1637+3631 is enhanced in IMEs, in apparent contrast to the results of Wong et al. (2024) who instead found the ejecta to be dominated by iron group elements (IGEs). However, their short timescale hydrodynamical simulations only cover the initial deposition of the IGE-dominated ejecta onto the donor, where the longer term evolution and radioactive decay of the accreted material is not considered. Their post-explosion evolutionary models using MESA (Modules for Experiments in Stellar Astrophysics) do not account for the accreted ejecta.

In conclusion, we find that SDSS J1637+3631 is *chemically* consistent as the donor of a D^6 supernova, where the observed abundances reflect the stripped core of a CO white dwarf, enhanced in Si- and Ca-rich supernova ejecta by 1–3 percent. Though we note some possible inconsistencies in the sulphur abundance and require the lowest velocity nickel-rich ejecta to be removed via radioactive decay powered winds.

4 CONFIRMING THE D^6 NATURE OF SDSS J1637+3631

In addition to the exotic atmospheric composition, the other key signature of D^6 remnants is their extreme kinematics with Galactic space motions exceeding 1000 km s^{-1} , resulting from their ejections from tight, double-degenerate binary systems. The radial velocity component of SDSS J1637+3631 is only around 400 km s^{-1} (Table 2), and is therefore insufficient to fully establish the D^6 nature. The tangential velocity, v_\perp , is instead required to confirm this scenario.

SDSS J1637+3631 has a moderate proper-motion at $|\mu| = 67.08 \pm 0.56\text{ mas yr}^{-1}$ (see Table 1), or equivalently $318 \pm 3\text{ km s}^{-1}\text{ kpc}^{-1}$. Ideally, the distance would be inferred from the *Gaia* parallax. As of *Gaia* DR3, however, the imprecise parallax of $0.3319 \pm 0.4776\text{ mas}$ is only sufficient to claim that SDSS J1637+3631 is at least $\sim 0.5\text{ kpc}$ from the Sun (at the 3σ level), and so space-motions ranging from only a few hundred to many thousands of km s^{-1} have near-equal likelihood, and are therefore kinematically consistent with a variety of explosion scenarios. Additional information is therefore needed to constrain the current distance and v_\perp of SDSS J1637+3631. Fortunately the spectroscopic $\log g$ serves this purpose, as it links the mass of SDSS J1637+3631, M_\star , to its radius, R_\star , which in turn constrains the distance, D , via the observed photometric fluxes and spectral model. Essentially, for some fixed solid-angle for the stellar disc, $M_\star \propto gD^2$. Therefore, if we require that $M_\star < 1.4\text{ M}_\odot$, and g is constrained by a measurement, an upper-bound can be placed on D . If a more informed prior on M_\star can be assumed, then the distances consistent with the data can be further refined.

To this end, we developed a simple Bayesian model to estimate the distance, mass, and radius of SDSS J1637+3631. The likelihood was constructed from the *Gaia* DR3 parallax, spectroscopic $\log g$,

and photometry (Table 1). Each photometric point was assumed to have a 0.01 mag systematic uncertainty in its absolute calibration in addition to the statistical errors, the latter of which is particularly small for the *Gaia* *G*-band. Additionally we included the T_{eff} and the interstellar reddening, $E(B - V)$, as nuisance parameters. For T_{eff} , we simply interpolated between our 1D grid of models which we previously used to estimate the T_{eff} uncertainty. For $E(B - V)$, we used the extinction model of [Gordon et al. \(2023\)](#), which we applied to our spectral model before calculating synthetic photometry by integrating over the appropriate pass bands. Each free parameter also requires careful consideration for its prior distribution. For the distance we assumed $P(D) \propto D^2$, reflecting a constant space density along the line of sight, which is a reasonable approximation for detectable objects close to the Galactic plane.³ For the mass, we assume that SDSS J1637+3631 was a normal CO core white dwarf (as evidenced by its spectrum) that lost some unknown fraction of its mass (e.g. due to donating mass to a companion, or from being stripped by supernova ejecta). We therefore adopted a prior distribution taking a two-component Gaussian mixture model for the white dwarf mass distribution (given by [O'Brien et al. 2024](#)), and convolved with a uniformly distributed fractional mass loss, i.e. replacing the Gaussian components with the corresponding Gaussian integrals. For the stellar radius, we assumed a log-uniform distribution between 10^{-3} and $1 R_{\odot}$. For the T_{eff} parameter, we used a Gaussian prior from the spectroscopic measurement, and finally for the reddening we used the Poisson Jeffreys prior of $P(E(B - V)) \propto E(B - V)^{-1/2}$.

To sample the posterior distribution, we used the PYTHON package `pocoMC` ([Karamanis et al. 2022b,a](#)), which uses a preconditioned Monte-Carlo (PMC) algorithm. This algorithm draws a specified number of particles from the prior distribution, $P(\theta)$, evolving the ensemble towards the posterior distribution $P(\theta|\mathbf{x})$ by gradually increasing an inverse-temperature, β , from 0 to 1 according to

$$P(\theta|\mathbf{x};\beta) \propto P(\theta)L(\mathbf{x}|\theta)^{\beta}, \quad (2)$$

where $L(\mathbf{x}|\theta)$ is the likelihood of the data \mathbf{x} with parameters θ . Furthermore, preconditioning is achieved at each step using a normalising flow, which allows the target distribution to be transformed to a simpler one that is easier to sample. Compared to other sampling methods such as Markov-Chain Monte-Carlo, the `pocoMC` implementation of PMC offers rapid convergence, while still performing well in complex (potentially multi-modal) parameter spaces, and with large numbers of free-parameters (a feature which is less relevant here, but which we exploit in the following section). Furthermore, `pocoMC` only requires prescriptions of the prior distribution and likelihood as inputs, without the need to supply analytical gradients (as in the case of techniques such as Hamiltonian Monte-Carlo). The online documentation⁴ and accompanying references (above) should be consulted for a more in depth description of the algorithm.

We sampled our model using the default `pocoMC` parameters (as of version 1.2.6). Specifically `n_effective=512`, `n_active=256`, which set the number of effective particles and active particles at each step, and also `flow='nsf6'` (neural spline flow with 6 transformations) for the choice of normalising-flow model. After convergence to $\beta = 1$, the total number of particles was allowed to grow to 16384

³ Beyond 10s of kpc, the Milky Way effectively becomes a point source for ejecting bound supernova remnants, at which point the density should drop off as D^{-2} . While this will result in a flat distance prior by itself, the limiting magnitude of *Gaia* will cause the distance distribution for *observable* D^6 stars to eventually drop to zero. This is discussed further in Section 5.4.

⁴ <https://github.com/minaskar/pocomc>
<https://pocomc.readthedocs.io/en/latest/>

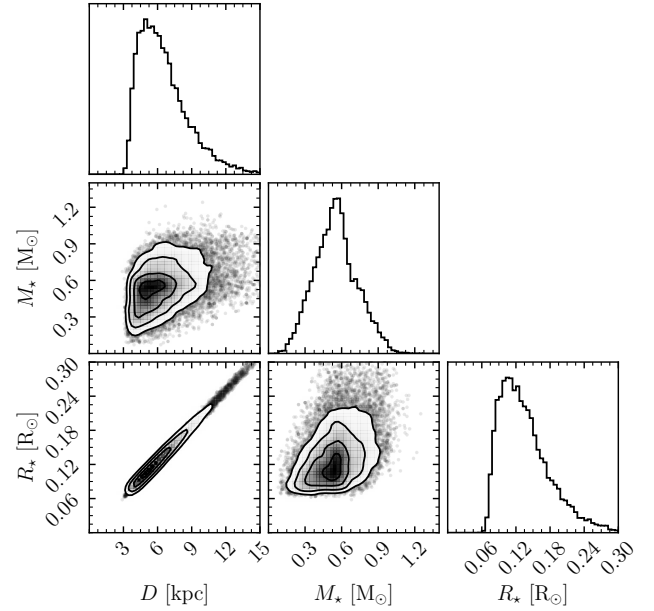


Figure 3. Corner plot to our fit to the distance, mass, and radius of SDSS J1637+3631, using the parallax, $\log g$, and photometry as constraints.

to provide a large number of samples from the posterior distribution. The corner plot for our parameters of interest, D , M_{\star} and R_{\star} are shown in Figure 3, where $D = 6.1^{+2.6}_{-1.6}$ kpc, $M_{\star} = 0.55^{+0.19}_{-0.17} M_{\odot}$, and $R_{\star} = 0.128^{+0.054}_{-0.034} R_{\odot}$. For the nuisance parameters, T_{eff} simply reflects the Gaussian prior, and has only a small correlation with the other nuisance parameter, $E(B - V)$, which was found to have a value of 0.086 ± 0.013 .

As hoped, the inclusion of $\log g$ in the likelihood and some simple assumptions about the range of feasible masses for SDSS J1637+3631 provides reasonable constraints on all three parameters. In particular, the distance is measured to approximately 3σ precision. Scaling by the proper-motion of $318 \pm 3 \text{ km s}^{-1} \text{ kpc}^{-1}$ therefore yields $v_{\perp} = 1950^{+810}_{-530} \text{ km s}^{-1}$. Combining this with the radial velocity gives a speed of $1980^{+790}_{-510} \text{ km s}^{-1}$ in the heliocentric reference frame. Transforming these samples to the Galactocentric frame gives a Galactic motion of $2070^{+790}_{-490} \text{ km s}^{-1}$. Therefore, in addition to the C+O composition enriched with nuclear burning products, this extreme velocity essentially confirms that SDSS J1637+3631 is indeed the ejected survivor of a D^6 explosion.

5 KINEMATIC ANALYSIS

In Section 4, we presented a Bayesian model incorporating the *Gaia* parallax, spectroscopic $\log g$, and photometry to constrain the distance, mass, radius, and interstellar reddening. This was in turn used to infer the Galactocentric velocity of SDSS J1637+3631 corroborating our earlier assertion that it was ejected from a D^6 supernova. With the distance and velocity samples in hand, it would be a relatively simple task to trace-back orbits to the point they cross the Galactic plane, thereby finding an approximate location of the explosion, and time of flight (assuming SDSS J1637+3631 to be ejected from the mid-plane of the disc). Such simulations have been performed for other runaway stars in the past ([Geier et al. 2015](#); [Raddi et al. 2018b](#);

Irrgang et al. 2018; Shen et al. 2018; Raddi et al. 2019; Ruffini & Casey 2019; Evans et al. 2020; El-Badry et al. 2023). However, by constraining the distance first and *then* constraining the ejection site as two separate steps, we lose any potential correlations between parameters of those separate calculations – or in other words, more precise parameters may be found by attempting to constrain the present distance and the ejection-site simultaneously. We also consider that the ejection-site should not be restricted to the Galactic mid-plane, and could instead occur above or below the plane, approximately proportional to the stellar density in the disc.

To that end, we extended our Bayesian model from before, incorporating Galactic dynamics in order to trace back SDSS J1637+3631 to its potential ejection site. We used the PYTHON package GALPY (Bovy 2015), which allows orbital integration using a variety of potentials including for within the Milky Way galaxy. We used the included MWPotential2014 potential in our calculations which consists of three components in order to model the disc, bulge, and halo. The disc is modelled with a Miyamoto-Nagai potential (Miyamoto & Nagai 1975), the bulge is modelled with a power law density profile with exponential cutoff (Bovy 2015), and the halo uses a Navarro-Frenk-White potential (Navarro et al. 1997). While we use ASTROPY for working with sky coordinates and conversions to the Galactocentric frame (Astropy Collaboration et al. 2013, 2018, 2022), internally GALPY works in a units system of natural units based on the distance to the Galactic centre, R , and the Sun’s Galactic orbital speed v . When converting to physical units, by default GALPY uses $R = 8$ kpc, and $v = 220 \text{ km s}^{-1}$. To improve compatibility with the ASTROPY Galactocentric frame, we instead used $R = 8.122$ kpc (GRAVITY Collaboration et al. 2018) for all conversions, taking care that this did not lead to any inconsistencies. Note that where ASTROPY uses a right-handed coordinate system, a left handed system is used by GALPY, and so further care was taken to ensure correctness throughout.

In addition to the five free parameters from before (Section 4), we included the three Galactocentric velocity components for SDSS J1637+3631 at its current location, $\mathbf{v} = (v_x, v_y, v_z)$, which were each given flat priors from -3000 km s^{-1} to $+3000 \text{ km s}^{-1}$. We also included a time of flight parameter, t , for integrating the past orbit of SDSS J1637+3631. From the distance posterior in Section 4 and Monte-Carlo sampling the proper-motion, we infer a value of $Z/v_z = 4.5 \pm 0.4 \text{ Myr}$ (where Z is the height above the Galactic plane in Galactocentric frame), which approximates the travel time from the mid-plane to the current location of SDSS J1637+3631. We therefore adopted a uniform prior from 0 to 10 Myr on t . Finally, a fractional parameter, f (with a uniform prior from 0 to 1), was also introduced to represent the mass fraction of the donor that survives the supernova, where the mass free-parameter from before now represents the donor mass at the time of detonation (denoted M_{don}), and where the current mass of SDSS J1637+3631 can be calculated as $M_\star = f M_{\text{don}}$. The need for this extra free parameter, f , will become apparent in a second simulation including tighter physical constraints. The priors on all parameters appearing in Section 4 remain unchanged.

Compared to before, the likelihood, L , is more complex, incorporating five independent components,

$$L = L_{\text{astrom}} \times L_{v_r} \times L_{\log g} \times L_{\text{phot}} \times \rho_{\text{ej}}, \quad (3)$$

with each term detailed below. Firstly, we introduce the *Gaia* astrometric likelihood $L_{\text{astrom}}(\varpi, \mu | D, \mathbf{v}; \Sigma)$, where ϖ is the parallax (corrected for the *Gaia* DR3 zero-point), μ is the proper motion (both components), and Σ is their covariance matrix including the off-diagonal terms provided by *Gaia*. L_{astrom} is simply a multivariate-

normal distribution where ASTROPY was used to perform coordinate conversion from distance and Galactocentric velocity to the estimated parallax and proper-motion to be compared with the measured values. The velocity to proper-motion conversion implicitly requires the right ascension and declination, though these were treated as fixed-values due to their sub-mas precision.

The spectroscopic radial-velocity, v_r , has a simple Gaussian likelihood written as $L_{v_r}(v_r | \mathbf{v}, M_{\text{don}}, f, R; \sigma_{v_r})$. The conversion from Galactocentric velocity components to inferred radial-velocity was performed as part of the previously described coordinate conversion. However, since the v_r measurement is independent of the other astrometry, we treat it as a separate likelihood term. We note that L_{v_r} also depends on M_{don} , f and R_\star , as the spectroscopic measurement includes both the relative motion and gravitational redshift. Whilst the values of M_\star and R_\star found in Section 4 imply a gravitational redshift of only a few km s^{-1} , this is comparable to our measurement uncertainty, and so should not be neglected.

The likelihood for the $\log g$ is similar to before, i.e. a Gaussian likelihood, but now $M_\star = f M_{\text{don}}$, and so this term now depends on three free-parameters rather than two. The photometric term in the likelihood remains unchanged, as it depends only on D , R_\star , T_{eff} , and $E(B - V)$, which were parameters in Section 4.

At this point, for a given D and \mathbf{v} , the model has no way to constrain t . The ejection site, $\mathbf{r}_0 = (X_0, Y_0, Z_0)$, is of course a function of D , \mathbf{v} and t , as they are the inputs to the orbital integration. However, we also wished to impose that the ejection site is more likely to be located in Galactic regions with higher stellar density. We therefore weighted the likelihood proportional to the mass-density in the Milky Way, i.e. $\rho_{\text{ej}}(D, \mathbf{v}, t) = \rho(\mathbf{r}_0(D, \mathbf{v}, t))$. While the mass-density within the Galaxy, and number density of binaries that could produce D^6 detonations need not be strictly proportional, the mass density is the more accessible quantity, and within the Galactic disc are likely to be similar. We calculated the mass density directly from the MWPotential2014 potential model within GALPY, where the library provides an analytic form for the potential components (without resorting to numerically calculating Poisson’s equation). However, we only used the bulge and disc components of the potential, ignoring the dark-matter dominated halo component. Formally ρ_{ej} is not a likelihood as the parameters do not define a distribution from which some data might be drawn. Instead it constitutes part of a joint prior on D , \mathbf{v} , and t , that restrict their possible combinations to those that originate from dense regions of the Galaxy. However, this joint prior is not trivial to sample in terms of D , \mathbf{v} , and t , which is required for the initialisation of our fitting approach. We therefore combined this with the likelihood terms for technical simplicity.

5.1 Results and ejection site location

As before, we used rocoMC to sample the posterior distribution,⁵ and using the same sampler parameters, and same final number of particles in the distribution. The best fitting values are given under ‘Fit 1’ in Table 3 (with the absence of T_{eff} , which once more simply reflects the Gaussian prior). Table 3 also includes other quantities derived from our fitted parameters: X_0 , Y_0 , and Z_0 are the coordinates inferred for the ejection site in Galactocentric coordinates, and ρ_{XY} , ρ_{XZ} , ρ_{YZ} are their correlation coefficients. Additionally, $v_{\text{gc}} = |\mathbf{v}|$ is the Galactocentric speed of SDSS J1637+3631 at the current epoch, and v_{ej} is the ejection speed of SDSS J1637+3631 after subtracting the component of Galactic orbital velocity at the

Parameter	Fit 0	Fit 1	Fit 2
D [kpc]	$6.1^{+2.6}_{-1.6}$	$5.4^{+0.9}_{-0.7}$	5.1 ± 0.4
v_x [km s $^{-1}$]		-1440^{+220}_{-260}	-1350 ± 120
v_y [km s $^{-1}$]		930^{+70}_{-60}	910 ± 30
v_z [km s $^{-1}$]		760^{+80}_{-70}	740 ± 40
t [Myr]		$4.5^{+0.4}_{-0.5}$	4.4 ± 0.4
M_{don} [M $_{\odot}$]		$0.56^{+0.20}_{-0.16}$	$0.57^{+0.18}_{-0.14}$
f		$0.79^{+0.15}_{-0.22}$	$0.78^{+0.16}_{-0.22}$
R_{\star} [R $_{\odot}$]	$0.128^{+0.054}_{-0.034}$	$0.114^{+0.019}_{-0.016}$	0.108 ± 0.009
$E(B - V)$	0.086 ± 0.013	0.086 ± 0.013	0.086 ± 0.013
X_0 [kpc]		$+0.4^{+2.0}_{-1.4}$	$+0.0 \pm 0.9$
Y_0 [kpc]		$-0.8^{+0.4}_{-0.3}$	-0.8 ± 0.4
Z_0 [kpc]		$+0.1^{+0.4}_{-0.3}$	$+0.1 \pm 0.3$
ρ_{XY}		-0.20	-0.49
ρ_{XZ}		-0.17	-0.48
ρ_{YZ}		$+0.973$	$+0.972$
$ r_0 $ [kpc]		$1.4^{+1.3}_{-0.6}$	$1.1^{+0.6}_{-0.3}$
v_{gc} [km s $^{-1}$]	2070^{+790}_{-490}	1870^{+280}_{-220}	1790 ± 120
v_{ej} [km s $^{-1}$]		1870^{+360}_{-300}	1750 ± 160
M_{\star} [M $_{\odot}$]	$0.55^{+0.19}_{-0.17}$	$0.42^{+0.17}_{-0.15}$	$0.41^{+0.17}_{-0.14}$
L_{\star} [L $_{\odot}$]	$0.89^{+0.91}_{-0.41}$	$0.70^{+0.25}_{-0.18}$	$0.63^{+0.11}_{-0.10}$

Table 3. Results from our orbital fits to SDSS J1637+3631. The explicitly fitted parameters are listed first. The second group refer to quantities derived from the fitted parameters. T_{eff} is not shown as the results simply reflect the measured prior, instead allowing more freedom in the other parameters such as $E(B - V)$. Parameters from Section 4 are listed under Fit 0 (note that M_{\star} is the fitted parameter here). Fit 1 represents our adopted parameters for SDSS J1637+3631, where the results from Fit 2 are potentially subject to uncertainties in the donor T_{eff} /radius at the time of explosion.

ejection site. Finally, M_{\star} is simply fM_{don} . A corner plot for D , v_{gc} , t , M_{don} , f , and M_{\star} is shown in Figure 4.

Compared to the results in Figure 3 (which are provided as Fit 0 in Table 3), the distance to SDSS J1637+3631 is refined to $5.4^{+0.9}_{-0.7}$ kpc.⁶ The improved precision on the distance is evident by comparing the top-left panels of Figures 3 and 4, which cover the same range of D values. Since v_{\perp} is directly proportional to the distance, the components of \mathbf{v} (and hence v_{gc}) are strongly correlated with D . The precision on the radius, R_{\star} , is improved by a similar amount to D , as they are also highly correlated. In contrast $E(B - V)$ shows no improvement as it depends only on the T_{eff} prior and the photometry which are unchanged.

Figure 5 shows the distribution of X_0 , Y_0 , and Z_0 within the Galaxy,

as well the trajectory taken by SDSS J1637+3631 to its current location. The distribution appears to overlap the Galactic centre when viewed in the X - Y and X - Z planes. Viewed from the Y - Z plane, however, it is clear that SDSS J1637+3631 cannot have originated from the Galactic centre. In essence, the posterior of X_0 , Y_0 , Z_0 is approximately an oblate Gaussian ellipsoid, whose orientation avoids it overlapping the Galactic centre. The volume enclosed by the 1σ Gaussian surface is 0.37 kpc^3 , calculated according to $\frac{4\pi}{3} |\Sigma_{XYZ}|^{1/2}$, where Σ_{XYZ} is the covariance matrix of X_0 , Y_0 , Z_0 , and can be constructed from the information provided in Table 3. We also calculated the probability that SDSS J1637+3631 originated from the disc versus the bulge. For each sample, i , we calculated the disc and bulge densities (ρ_{disc} and ρ_{bulge} , respectively) from the GALPY disc and bulge potentials. The probability that SDSS J1637+3631 was ejected from the disc, P_{disc} , is then given by

$$P_{\text{disc}} = \frac{1}{N} \sum_i \frac{\rho_{\text{disc}}(\mathbf{r}_{0,i})}{\rho_{\text{disc}}(\mathbf{r}_{0,i}) + \rho_{\text{bulge}}(\mathbf{r}_{0,i})}, \quad (4)$$

and similar for P_{bulge} . We subsequently found that SDSS J1637+3631 has a 83 percent probability of originating from the disc and a 17 percent probability of originating from the bulge.

5.2 Comparison with other objects and evolutionary models

With our refined estimate of D , we are now able to place SDSS J1637+3631 on the Hertzsprung-Russell diagram alongside other runaway white dwarfs and related stars. This is shown in Figure 6, where the solid red square corresponds to the *Gaia* DR3 photometry as given. We also show the location of SDSS J1637+3631 without reddening, with synthetic photometry calculated directly from our best fitting spectral model. Compared to the previously identified D⁶ stars, SDSS J1637+3631 sits between the redder/cooler objects found by Shen et al. (2018) and the bluer/hotter objects published by El-Badry et al. (2023), reflecting its intermediate T_{eff} . Although approximately double the T_{eff} of the cool D⁶ stars, SDSS J1637+3631 has a comparable absolute magnitude, indicating that its $0.1 R_{\odot}$ radius is smaller than those objects.

Shen (2025) recently calculated evolutionary tracks for the surviving donors of D⁶ supernovae. In their Figure 1, the fully convective CO donors initially contract almost isothermally at $T_{\text{eff}} \approx 6000 \text{ K}$, before eventually becoming radiative and evolving towards higher T_{eff} and briefly towards higher luminosities. Eventually their cores become degenerate, and the D⁶ stars return to the white dwarf cooling sequence. Our spectroscopic $T_{\text{eff}} = 15\,680 \pm 250$ combined with the inferred radius, $R_{\star} = 0.114^{+0.019}_{-0.016} R_{\odot}$, yields a luminosity of $L_{\star} = 0.70^{+0.25}_{-0.18} L_{\odot}$. These values imply a surviving donor mass of 0.18 – $0.20 M_{\odot}$ (Shen 2025, Figure 1) which is smaller than our estimate of $0.42^{+0.17}_{-0.15} M_{\odot}$, as given in Table 3. The cumulative distribution of our M_{\star} posterior samples has $0.2 M_{\odot}$ located at the 5th percentile. While this does not imply total disagreement between our derived mass and that from the evolutionary models of Shen (2025), it suggests that improvements to either our spectroscopic models (e.g. atomic data) or the evolutionary models calculated by Shen (2025) are required. Adopting our radius (constrained independently of the spectroscopic data) and assuming a mass of $0.2 M_{\odot}$ implies $\log g = 5.63 \text{ dex}$, which is more than 2σ below our spectroscopic measurement. On the other hand, altering the initial temperature, radius, and chemical profiles assumed by Shen (2025) will lead to different evolutionary tracks in the L - T_{eff} plane, which may permit higher masses for SDSS J1637+3631. Regardless of whether the masses can be made to agree, an even more egregious disagreement

⁵ In an earlier iteration of this model we had attempted to sample the posterior using MCMC methods such as EMCEE (Foreman-Mackey et al. 2013), however we found that the high-dimensionality of the problem caused slow convergence, with the distribution having barely burned in after several days of computation. Instead pocoMC allowed the posterior to be sampled in less than one hour on the same machine, permitting faster development.

⁶ As an interesting aside, because the distances involved are on the order of kpc, and the tangential velocity on the order 1000 km s^{-1} , the observed sky position significantly lags the true current location. At a distance of $5.4^{+0.9}_{-0.7} \text{ kpc}$, the light travel time is $18 \pm 3 \text{ kyr}$. Therefore SDSS J1637+3631 will have moved 31^{+11}_{-8} pc tangentially or $20 \pm 3 \text{ arcmin}$ since the observed light was emitted.

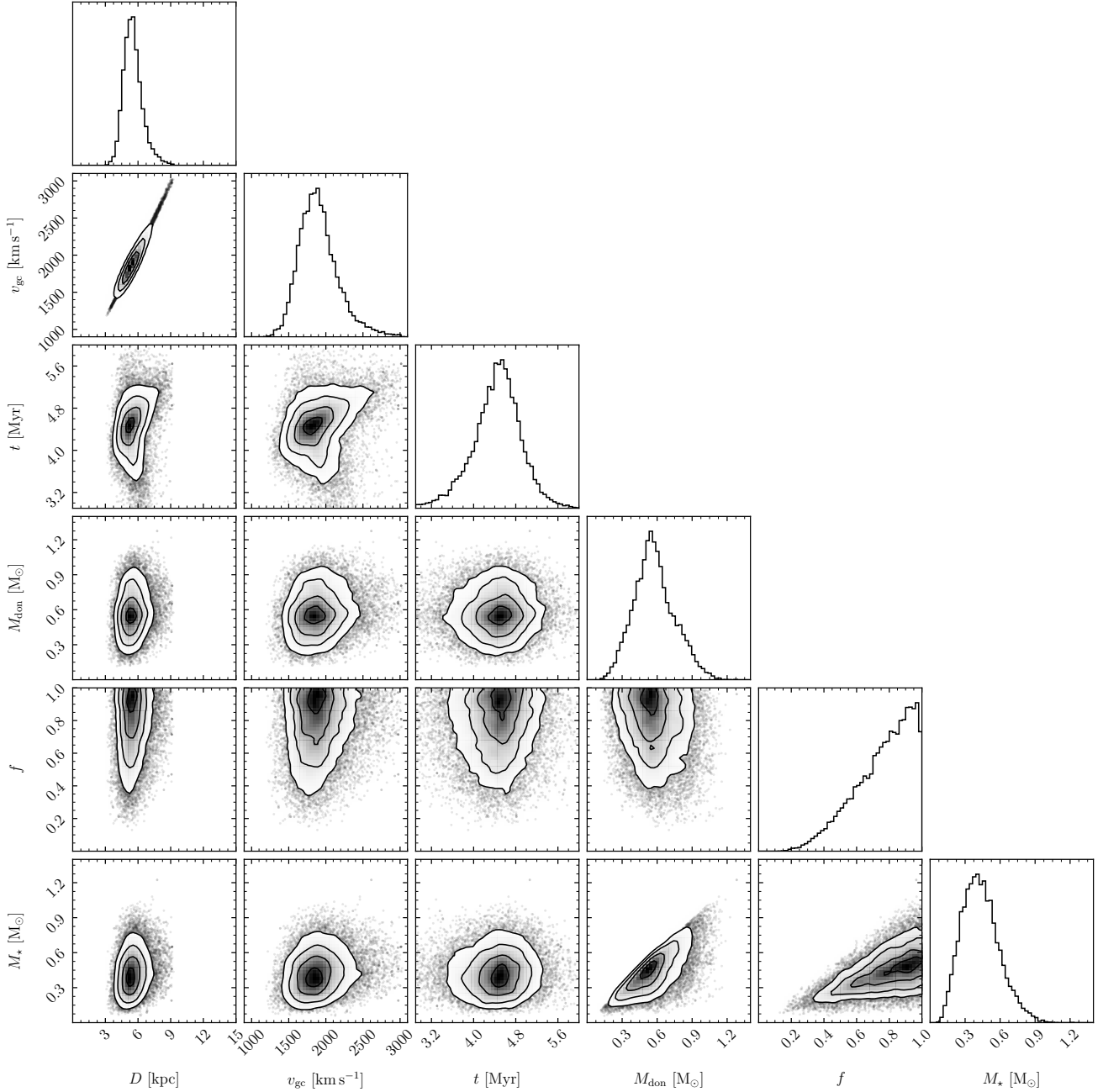


Figure 4. Corner plot for a subset of parameters in Fit 1. The derived parameter M_\star is also included, where $M_\star = fM_{\text{don}}$. Similarly v_{gc} is determined from the modulus of the individual components of \mathbf{v} . The distance, D , is shown over the same range as in Figure 3, demonstrating the substantial improvement in precision. M_{don} and M_\star are also shown over the same range as M_\star in Figure 3.

is seen in terms of age where our T_{eff} and luminosity imply a 12 Myr age according to the Shen (2025) tracks, in vast disagreement with our $4.5^{+0.4}_{-0.5}$ Myr time of flight.

Wong et al. (2024) and Bhat et al. (2025) have also performed evolutionary models for D^6 survivors. The helium white dwarf models of Wong et al. (2024) (see their Figure 8) appear quite different to the CO models of Shen (2025), where their tracks decrease in luminosity and radius over time, with a more gradual reduction in temperature. We note that for our ≈ 4.5 Myr time of flight, the tracks of Wong et al.

(2024) find approximately the correct radius to SDSS J1637+3631 of $\approx 0.1 R_\odot$, though at much lower T_{eff} . Given that these are helium white dwarf models, it is unsurprising that they disagree with the apparent CO core composition of SDSS J1637+3631. Bhat et al. (2025) investigated the inflated nature of the known D^6 remnants finding that the supernova shock heating could not maintain the inflated radii of the donors for more than $\sim 10^3$ yr – much shorter than the estimated age of SDSS J1637+3631 and the other known D^6 stars, implying some other mechanism is responsible for the large radii

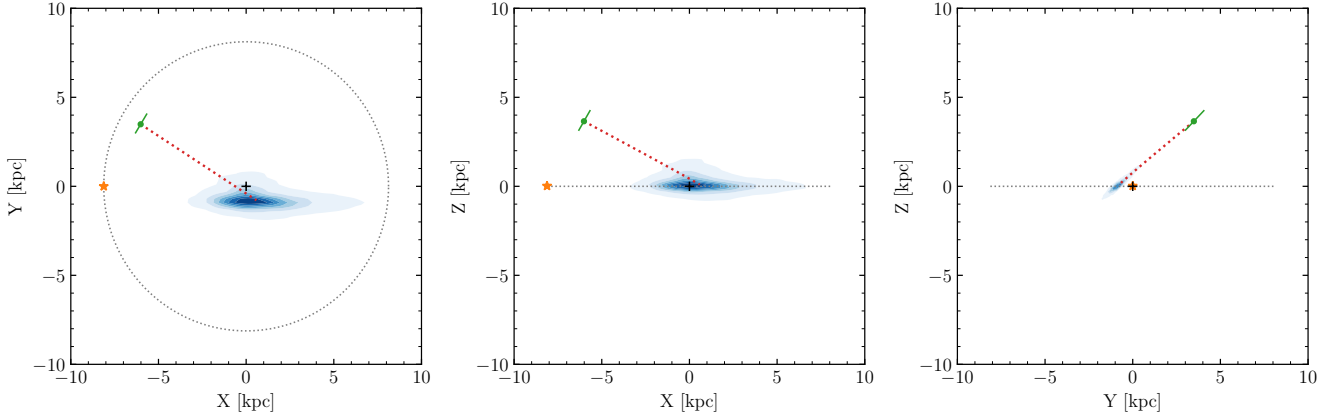


Figure 5. Ejection site and trajectory of SDSS J1637+3631 viewed along the three Cartesian axes, using posterior parameters from Fit 1. The current location of SDSS J1637+3631 and its distance uncertainty are shown by the green circle. The probability density for the ejection site is shown by the varying shades of blue. The trajectory for the median parameters is shown by the red dotted line. The black cross and orange star symbols indicate the location of the Galactic centre and Sun, respectively. The black dotted circle/lines correspond to the orbit of the Sun around the Milky Way.

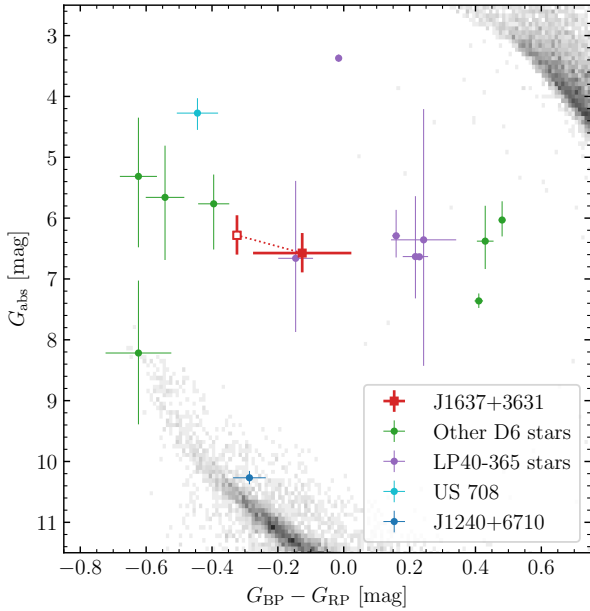


Figure 6. Hertzsprung-Russell diagram of runaway stars associated with supernovae. For SDSS J1637+3631, the distance used is from our kinematic analysis (Fit 1). The solid red square only uses the *Gaia* photometry and inferred distance, whereas the hollow square uses synthetic photometry from our best fitting spectral model, and thus excludes interstellar reddening. Objects identified by El-Badry et al. (2023) have been de-reddened by the values given therein. The white dwarf and main sequences are shown in grayscale.

of D⁶ remnants. At the ≈ 4.5 Myr age for SDSS J1637+3631 their models predict a radius that is an order of magnitude too low and a temperature several times too high (see their Figure 11), though these discrepancies cancel, yielding a luminosity estimate approximately correct for the age of SDSS J1637+3631. In summary, the disagreements between these evolutionary calculations and the results we

present here motivate further improvements to both the atmospheric and evolutionary models in order to resolve these tensions.

5.3 Constraining the ejection velocity from the donor mass

The velocity of the ejected donor reflects the orbital velocity at the time of the explosion,⁷ which is a function of the mass of both components in the binary. This idea has been explored by Bauer et al. (2021), and offers the potential to be applied to our kinematic analysis of SDSS J1637+3631 for refined results. Though the parameters we find here are more precise than those in Fit 1, they are also subject to the caveat of the unknown donor temperature, and so our results from Fit 1 should still be taken as our most reliable estimates.

Combining Kepler's third law, and the Roche lobe radius of the donor (Eggleton 1983), Bauer et al. (2021) showed that at the time of explosion, the orbital speed v_{orb} of the donor can be found via

$$v_{\text{orb}}^2 = \frac{0.49q^{2/3}GM_{\text{acc}}}{R_{\text{don}}(1+q)[0.6q^{2/3} + \ln(1+q^{1/3})]}, \quad (5)$$

where G is the gravitational constant, M_{acc} is the mass of the accreting primary, q is the mass ratio (i.e. $q = M_{\text{don}}/M_{\text{acc}}$), and R_{don} is the donor radius. Theory indicates that the D⁶ detonations should occur for primary masses between $0.85\text{--}1.15 M_{\odot}$, providing lower and upper-limits for M_{acc} (note that the accretor must also be at least as massive as the donor). Although the donor may have lost some fraction of its mass, it is still a white dwarf and should therefore still follow a standard white dwarf mass radius relation up to the detonation. Therefore R_{don} is a function of M_{don} , and so v_{orb} is also a function of M_{don} for both the lower and upper bounds of M_{acc} . An important caveat is that R_{don} is not just a function of M_{don} , but also the effective temperature of the donor, and the atmospheric composition. In the work of Bauer et al. (2021), they investigated a range

⁷ In principle the v_{ej} is a combination of v_{orb} and any kick, v_{kick} , imparted by the supernova, and so $v_{\text{ej}}^2 = v_{\text{orb}}^2 + v_{\text{kick}}^2$ (since any outward kick will be perpendicular to the direction of orbital motion). Unless the donor mass is particularly low (in which case v_{orb} will also be small), then the orbital component will dominate and the approximation $|v_{\text{ej}}| \approx |v_{\text{orb}}|$ is valid (see Figure 15 of El-Badry et al. 2023).

of T_{eff} and for both hydrogen and helium dominated atmospheres. For our analysis we assumed a helium dominated atmosphere as the dynamical instability leading to D^6 supernovae should not set in until after any hydrogen envelope is transferred. Similarly, the mass-radius relation for white dwarfs with He surfaces can still be sensitive to T_{eff} , but dynamical instability is most likely to set in and generate a supernova for more compact configurations with $T_{\text{eff}} \lesssim 30,000$ K, and the mass-radius relation is not particularly sensitive to temperature in this regime. Therefore, with no other obvious value available, we simply adopted the current spectroscopic T_{eff} of 15 680 K.

We used the [Bédard et al. \(2020\)](#) mass-radius relation to determine the R_{don} from M_{don} , and the current T_{eff} of SDSS J1637+3631. At this T_{eff} the [Bédard et al. \(2020\)](#) model grids provide valid results down to masses of $0.2 M_{\odot}$, which is already well covered by the posterior values of M_{don} in Figure 4. The upper and lower bounds on v_{orb} as a function of M_{don} were implemented as a prior which is flat between the bounds, but zero elsewhere. Here the reason to include f as a free parameter becomes apparent as this prior depends explicitly on M_{don} , but our likelihood terms for the surface gravity, and the gravitational redshift component of the spectroscopic radial velocity depend on the *current* mass of SDSS J1637+3631, M_{\star} . Therefore it is important to include a term representing any potential mass loss arising from interaction with the supernova ejecta, rather than assume these two masses to be identical.

The results from this fit are listed as Fit 2 in Table 3. The joint prior on v_{orb} and M_{don} limited the parameter space those quantities can occupy (Figure 7) improving the ejection velocity by around a factor of 2 (noting that we make the approximation $v_{\text{ej}} = v_{\text{orb}}$). Consequently several parameters that are sensitive to the ejection speed, have seen their uncertainties reduced by a similar amount, in particular D , R_{\star} , and the components of \mathbf{v} . The donor mass, M_{don} sees a comparatively marginal improvement, with similar small improvements seen for f and the derived M_{\star} . The time of flight, t , is minimally affected as it predominantly reflects the scale height of the disc at the inferred ejection site. The parameters T_{eff} and $E(B - V)$ show no improvement as the former is constrained only by its prior, and the latter only by the photometry, which remain unchanged here.

The inferred location of the ejection site (Figure 8) is also improved though with most of the improvement in X_0 , which also leads to increased correlation between X_0 and Y_0 , as well as X_0 and Z_0 (ρ_{XY} and ρ_{XZ} in Table 3). Once more, the posterior volume covered by these spatial parameters does not overlap the Galactic centre due to the strong correlation between Y_0 and Z_0 .

Employing these constraints, which are physically motivated by the properties of the binary at the time of explosion, greatly improves the precision of many quantities of interest. However, as this analysis depends on an arbitrarily chosen value of the donor T_{eff} at the explosion epoch, we reiterate that these results may be subject to additional uncertainties in the donor radius at time of explosion, and that the results from Fit 1 should be used when citing this work. Furthermore, [Braudo & Soker \(2024\)](#) has shown that the ejection velocity of the donor is typically reduced by 8–11 percent compared to its orbital velocity (due to the finite velocity of the supernova ejecta), an effect that has not been taken into account here, and may imply an even more massive value of M_{don} .

5.4 Future work for kinematic analyses

While the analyses performed throughout this section have been allowed us to determine several key properties of SDSS J1637+3631 (its ejection site, ejection velocity, and time of flight), our methodology is not without its limitations. Firstly, our distance prior,

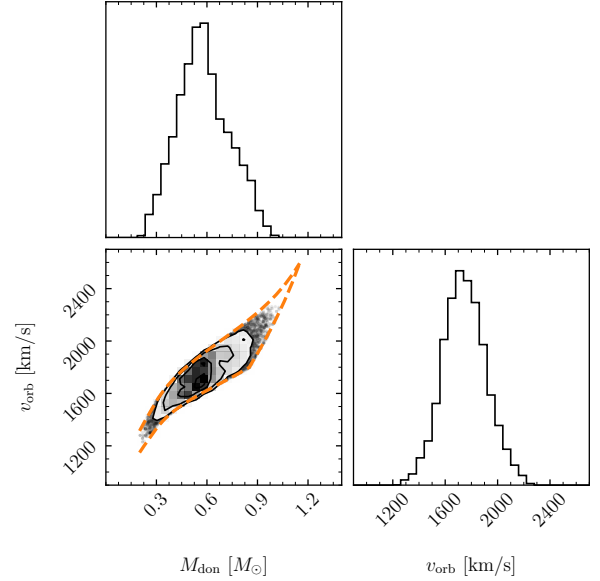


Figure 7. Corner plot for v_{orb} and M_{don} . The bounds inferred for $T_{\text{eff}} = 15\,680$ K are shown by the dashed lines.

$P(D) \propto D^2$, assumes a constant density of objects along the line of sight. This is likely to be true close to the Galactic plane, but will inevitably drop off at distances beyond a few kpc. At larger distances, the number of *detectable* D^6 stars will decrease as their apparent brightness will be too low for *Gaia*, but will depend on the evolutionary state of the specific object. A realistic distance prior will therefore require simulating the population of D^6 stars along different sight lines, considering for the distribution of ejection velocities, and potentially incorporating the evolving luminosity of the ejected donors ([Shen 2025](#)), if the disagreements presented above can be resolved. We therefore intend to explore this line of research in future work, though note that a preliminary investigation suggests the density of D^6 stars does not significantly drop for distances within 10 kpc along the sight line of SDSS J1637+3631.

As a further aside, our model presented earlier in this section integrates the path of SDSS J1637+3631 back towards a potential origin. However it is also possible to construct a forward model, where instead of the current distance as a free parameter, the ejection site \mathbf{r}_0 is used instead, and instead of the current velocity components, the velocity at ejection (\mathbf{v}_{ej}) is used. Clearly this approach introduces two additional free-parameters to the model, but also requires that the astrometric term in the likelihood include the *Gaia* RA and Dec and their uncertainties, otherwise the orbits are permitted to terminate at any sky coordinate. Such a model is attractive, as it completely removes the need for a distance prior, with the prior on \mathbf{r}_0 simply being the stellar density. While such a model is simple to implement, in practice we found that it was not possible to properly sample the posterior distribution, due to the covariance between parameters becoming almost singular. Consider the case that \mathbf{r}_0 is fixed: in order for the trajectory of the ejected donor to terminate within the cone described by the RA, Dec and uncertainties (sub-mas), extremely fine-tune parameters are needed for \mathbf{v}_{ej} and t , occupying a miniscule volume within the parameter space. A moderate change in \mathbf{r}_0 of say 0.5 kpc, will again lead to extremely fine-tuned, though

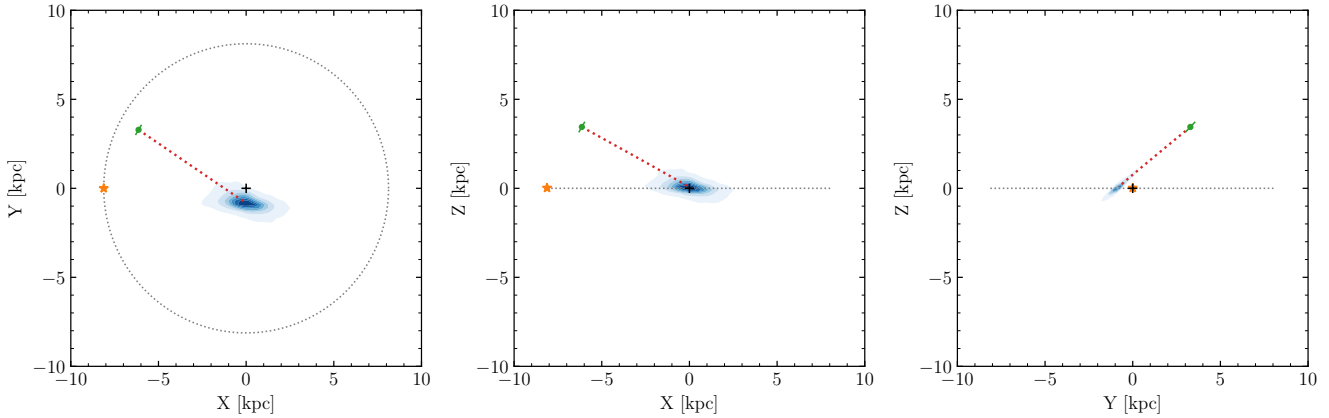


Figure 8. Ejection site and trajectory of SDSS J1637+3631 using posterior parameters from Fit 2. All symbols have the same meaning as in Figure 8.

substantially different parameters in order to once again land within the target volume defined by the astrometric likelihood. Therefore, when \mathbf{r}_0 is allowed to be free, the posterior density of \mathbf{r}_0 , \mathbf{v}_{ej} , and t essentially exists along a hyper-surface within the posterior hyper-volume. In our attempted implementation of the forward model, we were unable to find a way to deal with this correlation without affecting the posterior more generally: We tried artificially inflating the RA and Dec uncertainties, in order to increase the volume defined by the likelihood, but without substantially affecting the length of the integrated orbit (compared to the presumed uncertainty in \mathbf{r}_0). While this did reduce the extent of the parameter correlation, it also scaled the posterior for parameters relating to the orbit, and so no optimal value could be found. This is not to say that the forward model cannot successfully be implemented, but goes beyond the scope of this present work when adequate results can already be obtained from the reverse model.

Finally, the approach we have developed here can be applied more generally to other bound remnants of supernovae including both the D⁶ and LP40–365 stars. The analysis in this work represents an ideal case where SDSS J1637+3631 is high above the Galactic plane, a spectroscopic $\log g$ has been measured to restrict M_\star and R_\star , and a best fitting spectral model is available to compare against the photometry and constrain $E(B - V)$. For objects without spectroscopic analyses, as long as a full set of astrometry is available (including the radial velocity), it is still possible to constrain information about the ejection site, ejection velocity, and time of flight, though other important quantities such as the mass and radius will be inaccessible without further information. Analyses of other runaway stars is beyond the scope of this work, but will be investigated in the future.

6 CONCLUSIONS

SDSS J163712.21+363155.9 was previously identified from its peculiar spectrum hinting at a supernova origin, where we have now established it the surviving donor of a D⁶ type Ia supernova. Using our GTC observations, we performed the most detailed spectroscopic analysis of any D⁶ star to date, measuring the abundances for eight different elements. This revealed a C+O dominated atmosphere rich in IMEs such as Si, S, and Ca – a composition found to be consistent with an exposed CO white dwarf core enhanced by a few percent in the IME-rich ejecta of a double-detonation super-

nova. Despite a low-precision parallax, we were still able to infer a distance to SDSS J1637+3631 of ≈ 5 kpc and a Galactocentric velocity of $\approx 1900 \text{ km s}^{-1}$, corroborating the D⁶ explanation for SDSS J1637+3631. We then extended our analysis to explore the origin and kinematics of SDSS J1637+3631 in detail by tracing back its orbit, refining the distance and velocity measurements, and finding a time of flight of $4.5^{+0.4}_{-0.5}$ Myr. We found that SDSS J1637+3631 originated from the inner few kpc of the Galaxy, though the ejection site does not overlap the Galactic centre, and favours ejection from the disc population as opposed to the bulge. Finally, we refined this model further by restricting the ejection-speed based on the mass of the donor, as suggested by theoretical work, which we found led to even tighter constraints on the ejection site, ejection velocity and current distance from the Sun.

ACKNOWLEDGEMENTS

Based on observations made with the Gran Telescopio Canarias (GTC), installed in the Spanish Observatorio del Roque de los Muchachos of the Instituto de Astrofísica de Canarias (IAC), in the island of La Palma. This work is (partly) based on data obtained with the instrument OSIRIS, built by a Consortium led by the Instituto de Astrofísica de Canarias in collaboration with the Instituto de Astronomía de la Universidad Autónoma de México. OSIRIS was funded by GRANTECAN and the National Plan of Astronomy and Astrophysics of the Spanish Government. The Starlink software (Currie et al. 2014) is currently supported by the East Asian Observatory. This work made use of Astropy: (<https://www.astropy.org>) a community-developed core Python package and an ecosystem of tools and resources for astronomy (Astropy Collaboration et al. 2013, 2018, 2022). MAH acknowledges a Warwick Astrophysics prize post-doctoral fellowship made possible thanks to a generous philanthropic donation. Support for KJS was provided by NASA through the Astrophysics Theory Program (80NSSC20K0544) and by NASA/ESA Hubble Space Telescope program Nos. 15871, 15918, and 17441. RR acknowledges support from Grant RYC2021-030837-I, funded by MCIN/AEI/ 10.13039/501100011033 and by “European Union NextGeneration EU/PRTR”. This project has received funding from the European Research Council (ERC) under the European Union’s Horizon 2020 research and innovation programme (Grant agreement No. 101020057). This work was partially sup-

ported by the Spanish MINECO grant PID2023-148661NB-I00 and by the AGAUR/Generalitat de Catalunya grant SGR-386/2021. MAH acknowledges useful discussions with Stuart Littlefair on statistical methods, and Detlev Koester regarding their model atmosphere code. We thank the anonymous referee for their constructive feedback which improved the quality of this work.

DATA AVAILABILITY

All photometry and astrometry used in this work are publicly available (*Gaia*, SDSS, PanSTARRS). The raw GTC spectra can be found on the GTC archive with programme number GTC71-19A.

REFERENCES

- Astropy Collaboration et al., 2013, *A&A*, **558**, A33
 Astropy Collaboration et al., 2018, *AJ*, **156**, 123
 Astropy Collaboration et al., 2022, *ApJ Lett.*, **935**, 167
 Bauer E. B., Chandra V., Shen K. J., Hermes J. J., 2021, *ApJ Lett.*, **923**, L34
 Bédard A., Bergeron P., Brassard P., Fontaine G., 2020, *ApJ*, **901**, 93
 Bell G. S., Berry D. S., Graves S. F., Currie M. J., Draper P. W., 2024, in Hugo B. V., Van Rooyen R., Smirnov O. M., eds, *Astronomical Society of the Pacific Conference Series Vol. 535, Astronomical Data Analysis Software and Systems XXXI*. p. 455
 Bhat A., Bauer E. B., Pakmor R., Shen K. J., Caiazzo I., Rajamuthukumar A. S., El-Badry K., Kerzendorf W. E., 2025, *A&A*, **693**, A114
 Boos S. J., Townsley D. M., Shen K. J., Caldwell S., Miles B. J., 2021, *ApJ*, **919**, 126
 Boos S. J., Townsley D. M., Shen K. J., 2024, *ApJ*, **972**, 200
 Bovy J., 2015, *ApJS*, **216**, 29
 Braudo J., Soker N., 2024, *The Open Journal of Astrophysics*, **7**, 7
 Chandra V., et al., 2022, *MNRAS*, **512**, 6122
 Cunto W., Mendoza C., Ochsenbein F., Zeippen C. J., 1993, *A&A*, **275**, L5
 Currie M. J., Berry D. S., Jenness T., Gibb A. G., Bell G. S., Draper P. W., 2014, in Manset N., Forshay P., eds, *Astronomical Society of the Pacific Conference Series Vol. 485, Astronomical Data Analysis Software and Systems XXIII*. p. 391
 Dan M., Rosswog S., Guillochon J., Ramirez-Ruiz E., 2011, *ApJ*, **737**, 89
 Eggleton P. P., 1983, *ApJ*, **268**, 368
 El-Badry K., et al., 2023, *The Open Journal of Astrophysics*, **6**, 28
 Evans F. A., Renzo M., Rossi E. M., 2020, *MNRAS*, **497**, 5344
 Fink M., Hillebrandt W., Röpke F. K., 2007, *A&A*, **476**, 1133
 Fink M., Röpke F. K., Hillebrandt W., Seitenzahl I. R., Sim S. A., Kromer M., 2010, *A&A*, **514**, A53
 Fink M., et al., 2014, *MNRAS*, **438**, 1762
 Foley R. J., et al., 2013, *ApJ*, **767**, 57
 Foreman-Mackey D., Hogg D. W., Lang D., Goodman J., 2013, *PASP*, **125**, 306
 GRAVITY Collaboration et al., 2018, *A&A*, **615**, L15
 Gänsicke B. T., Koester D., Raddi R., Toloza O., Kepler S. O., 2020, *MNRAS*, **496**, 4079
 Geier S., et al., 2015, *Sci*, **347**, 1126
 Gordon K. D., Clayton G. C., Decleir M., Fitzpatrick E. L., Massa D., Misselt K. A., Tollerud E. J., 2023, *ApJ*, **950**, 86
 Guillochon J., Dan M., Ramirez-Ruiz E., Rosswog S., 2010, *ApJ Lett.*, **709**, L64
 Hermes J. J., Putterman O., Hollands M. A., Wilson D. J., Swan A., Raddi R., Shen K. J., Gänsicke B. T., 2021, *ApJ Lett.*, **914**, L3
 Hills J. G., 1988, *Nat*, **331**, 687
 Hollands M. A., et al., 2020, *Nat Astron.*, **4**, 663
 Horne K., 1986, *PASP*, **98**, 609
 Igoshev A. P., Perets H., Hallakoun N., 2023, *MNRAS*, **518**, 6223
 Irrgang A., Kreuzer S., Heber U., 2018, *A&A*, **620**, A48
 Jha S., Branch D., Chornock R., Foley R. J., Li W., Swift B. J., Casebeer D., Filippenko A. V., 2006, *AJ*, **132**, 189
 Jones S., et al., 2019, *A&A*, **622**, A74
 Karamanis M., Nabergoj D., Beutler F., Peacock J., Seljak U., 2022a, *J. Open Source Softw.*, **7**, 4634
 Karamanis M., Beutler F., Peacock J. A., Nabergoj D., Seljak U., 2022b, *MNRAS*, **516**, 1644
 Kepler S. O., et al., 2016, *MNRAS*, **455**, 3413
 Khokhlov A. M., 1991, *A&A*, **245**, 114
 Kilic M., Bergeron P., Blouin S., Jewett G., Brown W. R., Moss A., 2024, *ApJ*, **965**, 159
 Koester D., 2010, *Memorie della Societa Astronomica Italiana*, **81**, 921
 Kposov S. E., et al., 2020, *MNRAS*, **491**, 2465
 Kramida A., Yu. Ralchenko Reader J., and NIST ASD Team 2024, NIST Atomic Spectra Database (ver. 5.12), [Online]. Available: <https://physics.nist.gov/asd> [2025, March 13]. National Institute of Standards and Technology, Gaithersburg, MD.
 Kromer M., et al., 2013, *MNRAS*, **429**, 2287
 Li W., et al., 2003, *PASP*, **115**, 453
 Livne E., 1990, *ApJ Lett.*, **354**, L53
 Marsh T. R., 1989, *PASP*, **101**, 1032
 McCully C., et al., 2014, *Nat*, **512**, 54
 Miyamoto M., Nagai R., 1975, *PASJ*, **27**, 533
 Navarro J. F., Frenk C. S., White S. D. M., 1997, *ApJ*, **490**, 493
 O’Brien M. W., et al., 2024, *MNRAS*, **527**, 8687
 Pakmor R., Kromer M., Taubenberger S., Springel V., 2013, *ApJ Lett.*, **770**, L8
 Pakmor R., et al., 2022, *MNRAS*, **517**, 5260
 Perlmutter S., et al., 1999, *ApJ*, **517**, 565
 Raddi R., Hollands M. A., Koester D., Gänsicke B. T., Gentile Fusillo N. P., Hermes J. J., Townsley D. M., 2018a, *ApJ*, **858**, 3
 Raddi R., Hollands M. A., Gänsicke B. T., Townsley D. M., Hermes J. J., Gentile Fusillo N. P., Koester D., 2018b, *MNRAS*, **479**, L96
 Raddi R., et al., 2019, *MNRAS*, **489**, 1489
 Raskin C., Scannapieco E., Fryer C., Rockefeller G., Timmes F. X., 2012, *ApJ*, **746**, 62
 Riess A. G., et al., 1998, *AJ*, **116**, 1009
 Ruffini N. J., Casey A. R., 2019, *MNRAS*, **489**, 420
 Ruiter A. J., Seitenzahl I. R., 2025, *A&AR*, **33**, 1
 Scholz R. D., 2024, *A&A*, **685**, A162
 Seitenzahl I. R., Cescutti G., Röpke F. K., Ruiter A. J., Pakmor R., 2013, *A&A*, **559**, L5
 Shen K. J., 2025, *ApJ*, **982**, 6
 Shen K. J., Bildsten L., 2014, *ApJ*, **785**, 61
 Shen K. J., Schwab J., 2017, *ApJ*, **834**, 180
 Shen K. J., Idan I., Bildsten L., 2009, *ApJ*, **705**, 693
 Shen K. J., et al., 2018, *ApJ*, **865**, 15
 Shen K. J., Boos S. J., Townsley D. M., 2024, *ApJ*, **975**, 127
 Shields J. V., Arunachalam P., Kerzendorf W., Hughes J. P., Biriouk S., Monk H., Buchner J., 2023, *ApJ Lett.*, **950**, L10
 Taam R. E., 1980, *ApJ*, **242**, 749
 Tanikawa A., Nomoto K., Nakasato N., Maeda K., 2019, *ApJ*, **885**, 103
 Thielemann F. K., Nomoto K., Yokoi K., 1986, *A&A*, **158**, 17
 Vennes S., Nemeth P., Kawka A., Thorstensen J. R., Khalack V., Ferrario L., Alper E. H., 2017, *Sci*, **357**, 680
 Wang B., Han Z., 2012, *New Astron. Rev.*, **56**, 122
 Werner K., Reindl N., Rauch T., El-Badry K., Bédard A., 2024a, *A&A*, **682**, A42
 Werner K., El-Badry K., Gänsicke B. T., Shen K. J., 2024b, *A&A*, **689**, L6
 Wong T. L. S., White C. J., Bildsten L., 2024, *ApJ*, **973**, 65

This paper has been typeset from a \LaTeX file prepared by the author.